photonics

Article

Wide-Angle Absorption Based on Angle-Insensitive Light Slowing Effect in Photonic Crystal Containing Hyperbolic Metamaterials

Feng Wu [1,*], Xiaoqing Li [1], Xiufeng Fan [1], Ling Lin [1], Sofyan A. Taya [2] and Abinash Panda [3]

[1] School of Optoelectronic Engineering, Guangdong Polytechnic Normal University, Guangzhou 510665, China; lxq13612398470@163.com (X.L.); fxf_paula@163.com (X.F.); eve1239806077@163.com (L.L.)
[2] Physics Department, Islamic University of Gaza, Gaza P.O. Box 108, Palestine; staya@iugaza.edu.ps
[3] Department of Electronics and Communication Engineering, National Institute of Technology Silchar, Silchar 788010, Assam, India; abinash_rs@ece.nits.ac.in
* Correspondence: fengwu@gpnu.edu.cn

Abstract: Light-slowing effect at band edges in photonic crystals (PCs) is widely utilized to enhance optical absorption. However, according to the Bragg scattering theory, photonic bandgaps (PBGs) in traditional all-dielectric one-dimensional (1-D) PCs shift towards shorter wavelengths as the incident angle increases. Therefore, light-slowing effect in traditional all-dielectric 1-D PCs is also angle-sensitive. Such angle-sensitive property of light-slowing effect in traditional all-dielectric 1-D PCs poses a great challenge to achieve wide-angle absorption. In this paper, we design an angle-insensitive PBG in a 1-D PC containing hyperbolic metamaterials based on the phase-variation compensation theory. Assisted by the angle-insensitive light-slowing effect at the angle-insensitive band edge, we achieve wide-angle absorption at near-infrared wavelengths. The absorptance keeps higher than 0.9 in a wide angle range from 0 to 45.5 degrees. Besides, the wide-angle absorption is robust when the phase-variation compensation condition is slightly broken. Our work not only provides a viable route to realize angle-insensitive light slowing and wide-angle light absorption, but also promotes the development of light-slowing- and absorption-based optical/optoelectronic devices.

Keywords: photonic crystal; hyperbolic metamaterial; photonic bandgap; band edge; light slowing; absorption

check for updates

Citation: Wu, F.; Li, X.; Fan, X.; Lin, L.; Taya, S.A.; Panda, A. Wide-Angle Absorption Based on Angle-Insensitive Light Slowing Effect in Photonic Crystal Containing Hyperbolic Metamaterials. *Photonics* **2022**, *9*, 181. https://doi.org/10.3390/photonics9030181

Received: 18 February 2022
Accepted: 11 March 2022
Published: 12 March 2022

1. Introduction

Optical absorption plays an important role in various optical/optoelectronic devices, such as solar cells [1,2], photodetectors [3,4], sensors [5,6], and gas analyzers [7,8]. Over the past two decades, a series of resonant microstructures have been proposed to enhance optical absorption [9–20]. Particularly, researchers discovered that light-slowing effect can occur at the band edges in photonic crystals (PCs) [21–23]. Assisted by the light-slowing effect at the band edges, optical absorption can be greatly enhanced [24–27]. As a typical kind of PC, all-dielectric one-dimensional (1-D) PCs have attracted great interest [28–32] since they can be easily fabricated by the electro-beam vacuum deposition [33] and the magnetron sputtering techniques [34]. However, according to the Bragg scattering theory, photonic bandgaps (PBGs) in traditional all-dielectric 1-D PCs will shift towards shorter wavelengths (i.e., angle-sensitive) as the incident angle increases [28,33–37]. Therefore, light-slowing effect in traditional all-dielectric 1-D PCs is also angle-sensitive, which poses a challenge to achieve wide-angle absorption. To date, how to achieve angle-insensitive-light-slowing effect in 1-D PCs has remained an open theoretical problem. If one can achieve angle-insensitive light-slowing effect in 1-D PCs, wide-angle absorption can also be realized.

Over the past decade, a kind of strongly anisotropic metamaterial called hyperbolic metamaterials (HMMs) has attracted immense attention since they possess potential applications in PBG engineering [38–41], spontaneous emission controlling [42], perfect absorbers [43,44], and lasers [45]. Particularly, by introducing HMMs into 1-D PCs, researchers realized a new class of PBGs called angle-insensitive PBGs under transverse magnetic (TM) polarization [46–48]. Such special 1-D PCs can be called 1-D PCs containing HMMs (PCCHs). Different from blueshift PBGs in traditional all-dielectric 1-D PCs, band edges of angle-insensitive PBGs in 1-D PCCHs remain almost unshifted as the incident angle increases [46–48]. The angle-insensitive property of PBGs in 1-D PCCHs provides us a possibility to achieve angle-insensitive light slowing effect. In this paper, we design an angle-insensitive PBG in a 1-D PCCH based on the phase-variation compensation theory in [46]. Then, we utilize the angle-insensitive light slowing effect at the angle-insensitive band edge in the designed 1-D PCCH to achieve wide-angle absorption at near-infrared wavelengths. At the short-wavelength angle-insensitive band edge ($\lambda = 1702.0$ nm), the absorptance keeps higher than 0.9 in a wide angle range from 0° to 45.5°. Compared with the reported wide-angle absorbers based on 2-D and 3-D structures [19,49,50], the proposed wide-angle absorber based on 1-D lithography-free structure can greatly reduce the fabrication costs. Next, we also prove that the wide-angle absorption is robust when the phase-variation compensation condition is slightly broken. Our work not only provides a viable route to realize angle-insensitive light slowing and wide-angle light absorption, but also promotes the development of light-slowing- and absorption-based optical/optoelectronic devices.

This paper is organized as follows. In Section 2, we recall the angle-sensitive property of the absorption based on the light slowing effect at the band edge in traditional all-dielectric 1-D PC. In Section 3, we design an angle-insensitive PBG in a 1-D PCCH based on the phase-variation compensation theory in [46] and then utilize the angle-insensitive light slowing effect at the angle-insensitive band edge to achieve wide-angle absorption at near-infrared wavelengths. Besides, we change the layer thickness to slightly break the phase-variation compensation condition to analyze the robustness of the wide-angle absorption. Finally, the conclusion is given in Section 4.

2. Angle-Sensitive Absorption Based on Light Slowing Effect at Band Edge in Traditional All-Dielectric 1-D PC

In this section, we recall the angle-sensitive property of the absorption based on the light-slowing effect at band edge in traditional all-dielectric 1-D PC. The all-dielectric 1-D PC can be denoted by $(AB)^{10}$. The refractive indices of dielectrics A and B are set to be $n_A = 1.5$ and $n_B = 2.5$, respectively. The thicknesses of A and B layers are set to be $d_A = 270.0$ nm and $d_B = 240.0$ nm, respectively. According to the transfer matrix method [51], we write a MATLAB code to calculate the transmittance spectrum of the all-dielectric 1-D PC $(AB)^{10}$ at normal incidence under TM polarization, as shown in Figure 1a. According to the boundary conditions of the electromagnetic fields, the transfer matrix of a layer can be represented by a 2×2 matrix. Then, the total matrix of the whole structure can be expressed as the product of the transfer matrices of all the layers. Next, the transmittance/reflectance/absorptance spectra can be calculated by the elements of the total transfer matrix. The incident medium is set to be air and the exit medium (substrate) is set to be BK7 glass with a refractive index $n_S = 1.515$ [52]. One can see that a PBG emerges in the wavelength range from 1699.9 to 2469.0 nm. The short- and the long-wavelength band edges are marked by P1 and P2 in Figure 1a. To show the absorption property of the band edges, we add the material loss into the lossless all-dielectric 1-D PC to construct a lossy all-dielectric 1-D PC. Now, the refractive index of dielectric B is selected to be $n_B = 2.5 + 0.08i$. Figure 1b give the absorptance spectrum of the lossy all-dielectric 1-D PC $(AB)^{10}$ at normal incidence under TM polarization. One can see that two absorptance peaks emerge at the short- and the long-wavelength band edges. Specifically, the peak values of two absorptance peaks reach 0.712 and 0.609. To confirm that the absorptance peaks originate from the light-slowing effect, here we calculate the group refractive index n_g based on the theory in [53]. The real part of the effective refractive index of the 1-D PC can be calculated by [53]

$$\mathrm{Re}[n_{\mathrm{eff}}(\omega)] = \frac{\arg[t(\omega)]c}{d_{\mathrm{Total}}\omega}, \tag{1}$$

where $t(\omega)$ represents the transmission coefficient of the 1-D PC, c represents the light velocity in vacuum, ω represents the angular frequency of the incident light, and d_{Total} represents the total thickness of the 1-D PC, respectively. Then, the group refractive index of the 1-D PC can be calculated by [53]

$$n_g(\omega) = \mathrm{Re}[n_{\mathrm{eff}}(\omega)] + \omega \frac{\mathrm{d}\{\mathrm{Re}[n_{\mathrm{eff}}(\omega)]\}}{\mathrm{d}\omega}. \tag{2}$$

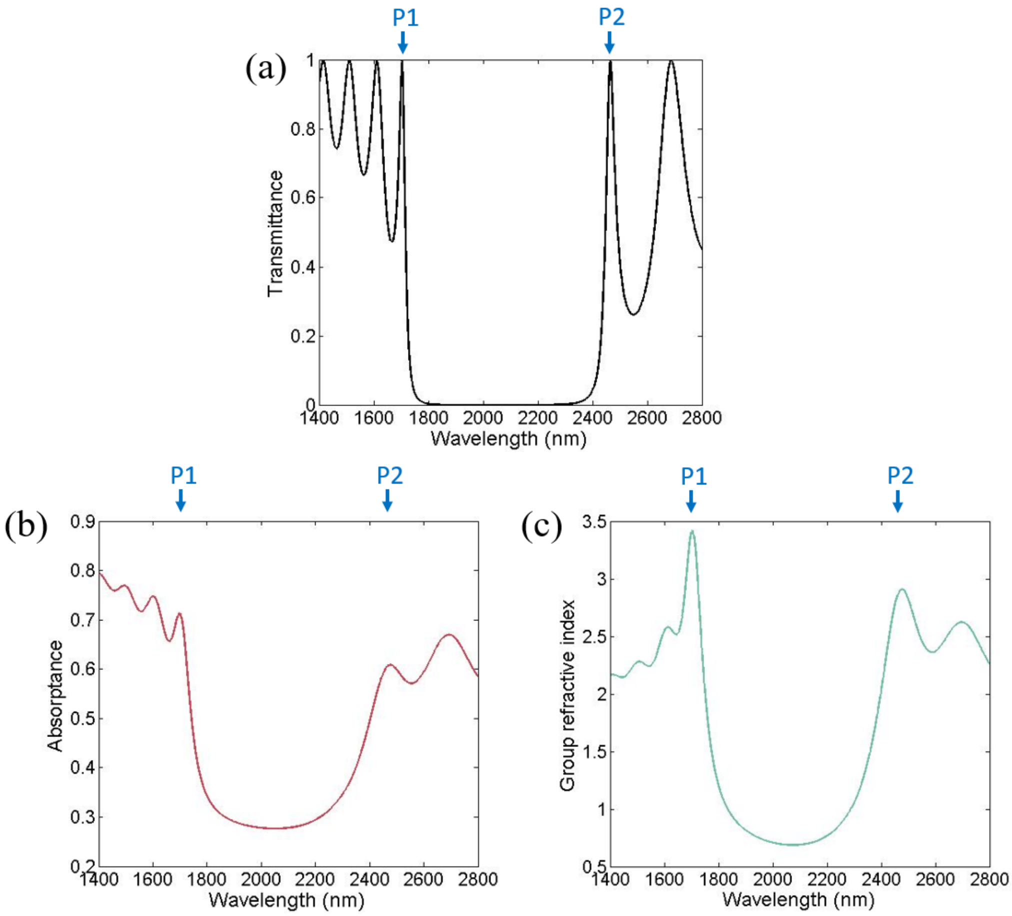

Figure 1. (**a**) Transmittance spectrum of the lossless all-dielectric 1-D PC $(AB)^{10}$ at normal incidence under TM polarization. (**b**) Absorptance and (**c**) group refractive index spectra of the lossy all-dielectric 1-D PC $(AB)^{10}$ at normal incidence under TM polarization.

According to Equations (1) and (2), we calculate the group refractive index spectrum of the lossy all-dielectric 1-D PC $(AB)^{10}$ at normal incidence under TM polarization in Figure 1c. Clearly, at two band edges, the group refractive indices are greatly enhanced to 3.418 and 2.908, respectively. The corresponding group velocities are only 0.293c and 0.344c, respectively. Hence, two absorptance peaks originate from the light-slowing effect at two band edges.

Now we discuss the angle-dependence of the absorption. Figure 2a gives the absorptance spectrum of the lossy all-dielectric 1-D PC $(AB)^{10}$ as a function of the incident angle under TM polarization. One can clearly see that as the incident angle increases, the PBG strongly shifts towards shorter wavelengths. Therefore, two absorptance peaks (shown by blue dashed lines) will also shift towards shorter wavelengths. Specifically, as the incident angle increases from 0° to 60°, the short-wavelength absorptance peak strongly shifts from 1698.4 to 1557.7 nm and the long-wavelength one strongly shifts from 2476.3 to 2100.7 nm. Figure 2b also gives the group refractive index spectrum of the lossy all-dielectric 1-D PC $(AB)^{10}$ as a function of the incident angle under TM polarization. As demonstrated, two group refractive index peaks exhibit blueshift property. Such angle-sensitive property of the light slowing effect gives rise to the angle-sensitive property of the absorptance peaks.

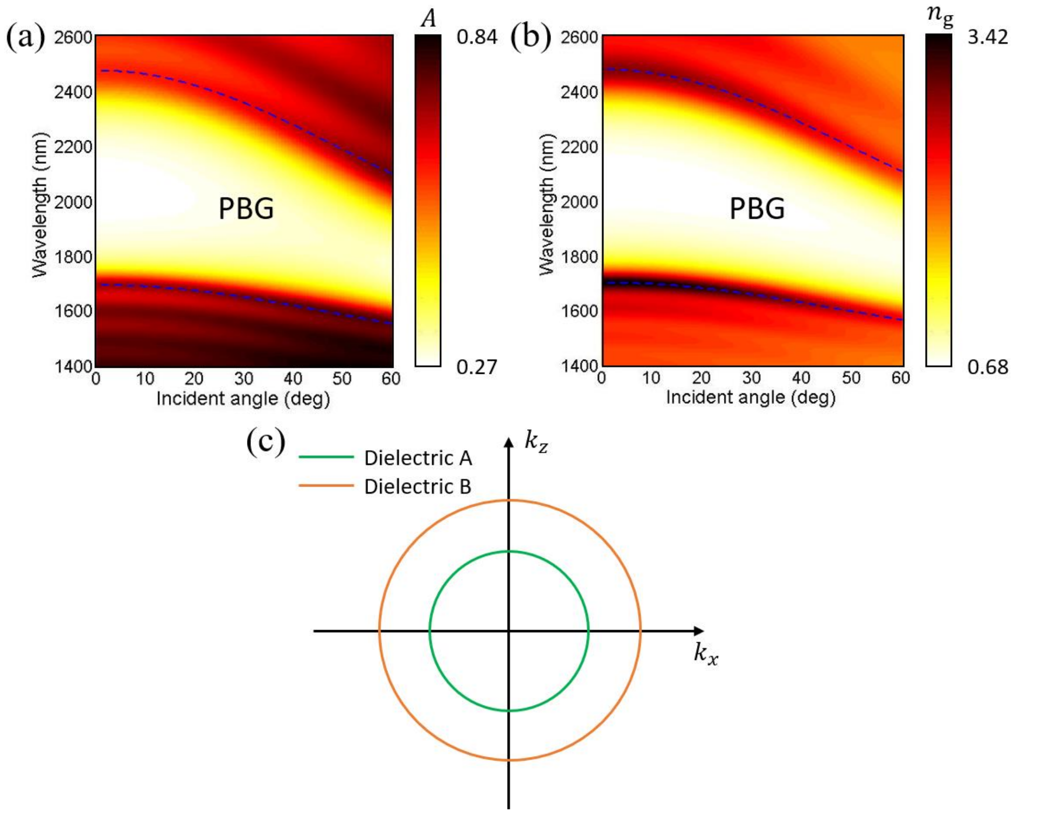

Figure 2. (**a**) Absorptance and (**b**) group refractive index spectra of the lossy all-dielectric 1-D PC $(AB)^{10}$ as a function of the incident angle under TM polarization. (**c**) IFCs of dielectrics A and B under TM polarization.

The blueshift property of the PBG in all-dielectric 1-D PC can be explained by the Bragg scattering theory. It is known that the propagating phase within a unit cell of the all-dielectric 1-D PC can be expressed as functions of the wavelength and the incident angle, i.e.,

$$\Phi(\lambda,\theta) = k_{\mathrm{A}z}(\lambda,\theta)d_{\mathrm{A}} + k_{\mathrm{B}z}(\lambda,\theta)d_{\mathrm{B}}, \tag{3}$$

where $k_{\mathrm{A}z}$ and $k_{\mathrm{B}z}$ represent the z components (perpendicular to the interface) of the wave vectors within dielectrics A and B, respectively. Substituting the relative permittivity of dielectric A or B (ε_{A} or ε_{B}) into the Maxwell equations, we obtain the equation of the iso-frequency curve (IFC) of dielectric A or B under TM polarization [54]

$$\frac{k_x^2}{\varepsilon_{\mathrm{A}}} + \frac{k_{\mathrm{A}z}^2}{\varepsilon_{\mathrm{A}}} = k_0^2 = \left(\frac{2\pi}{\lambda}\right)^2, \tag{4}$$

$$\frac{k_x^2}{\varepsilon_{\mathrm{B}}} + \frac{k_{\mathrm{B}z}^2}{\varepsilon_{\mathrm{B}}} = k_0^2 = \left(\frac{2\pi}{\lambda}\right)^2, \tag{5}$$

where k_x represents the x components (parallel to the interface) of the wave vector and k_0 represents the wave vector in vacuum. From Equations (4) and (5), both the IFCs of dielectrics A and B are circles, as schematically shown in Figure 2c.

Then, substituting $k_x = k_0 \sin\theta$ into Equations (4) and (5), we obtain

$$k_{\mathrm{Az}} = \frac{2\pi}{\lambda}\sqrt{\varepsilon_{\mathrm{A}} - \sin^2\theta}. \tag{6}$$

$$k_{\mathrm{Bz}} = \frac{2\pi}{\lambda}\sqrt{\varepsilon_{\mathrm{B}} - \sin^2\theta}. \tag{7}$$

Next, substituting Equations (6) and (7) into Equation (3), we can finally obtain

$$\Phi(\lambda,\theta) = \frac{2\pi}{\lambda}\left(d_{\mathrm{A}}\sqrt{\varepsilon_{\mathrm{A}} - \sin^2\theta} + d_{\mathrm{B}}\sqrt{\varepsilon_{\mathrm{B}} - \sin^2\theta}\right). \tag{8}$$

From Equation (8), we have $\partial\Phi/\partial\lambda < 0$ and $\partial\Phi/\partial\theta < 0$.

According to the Bragg scattering theory, the Bragg condition of the lowest-frequency PBG can be given by [55]

$$\Phi(\lambda_{\mathrm{Brg}},\theta) = \frac{2\pi}{\lambda_{\mathrm{Brg}}}\left(d_{\mathrm{A}}\sqrt{\varepsilon_{\mathrm{A}} - \sin^2\theta} + d_{\mathrm{B}}\sqrt{\varepsilon_{\mathrm{B}} - \sin^2\theta}\right) = \pi, \tag{9}$$

where λ_{Brg} represents the Bragg wavelength of the lowest-frequency PBG. As the incident angle increases, the Bragg wavelength λ_{Brg} must decrease to maintain the Bragg condition [Equation (9)] since $\partial\Phi/\partial\lambda < 0$ and $\partial\Phi/\partial\theta < 0$. Therefore, as the incident angle increases, the PBG in all-dielectric 1-D PC will shift towards shorter wavelengths. Equivalently, two band edges of the PBG will also shift towards shorter wavelengths.

In Figure 3, we calculate the absorptance of the lossy all-dielectric 1-D PC $(\mathrm{AB})^{10}$ as a function of the incident angle at the short-wavelength band edge $\lambda = 1698.4$ nm under TM polarization. One can see that the absorptance is sensitive to the incident angle due to the angle-sensitive property of the light-slowing effect at the short-wavelength band edge. As the incident angle increases from 0° to 80°, the absorptance rapidly decreases from 0.713 to 0.167. At an incident angle of 45°, the absorptance is only 0.419. The angular average absorptance in the angle range from 0° to 90° is only $\overline{A} = 0.433$. To sum up, the absorption based on the light slowing effect at band edge in traditional all-dielectric 1-D PC is angle-sensitive, which poses a great challenge to realize wide-angle absorption.

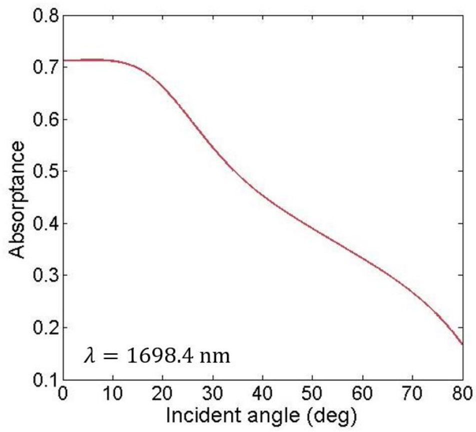

Figure 3. Absorptance of the lossy all-dielectric 1-D PC $(\mathrm{AB})^{10}$ as a function of the incident angle at the short-wavelength band edge $\lambda = 1698.4$ nm under TM polarization.

3. Wide-Angle Absorption Based on Angle-Insensitive Light Slowing Effect at Angle-Insensitive Band Edge in 1-D PCCH

In this section, we will achieve wide-angle absorption based on the angle-insensitive light slowing effect in an angle-insensitive band edge in a 1-D PCCH. First, we design an angle-insensitive PBG based on the phase-variation compensation theory in [46]. The 1-D PCCH is composed of alternating HMMs (C layers) and dielectrics (D layers). The HMM is mimicked by a subwavelength indium tin oxide (ITO)/silicon (Si) multilayer $(\mathrm{EF})^2$ and the dielectric is selected to be Si with a refractive index of $n_\mathrm{D} = 3.48$ [56]. The whole structure can be denoted by $[(\mathrm{EF})^2\mathrm{D}]^6$, as schematically shown in Figure 4a. As a candidate of plasmonic materials at near-infrared wavelengths, the relative permittivity of ITO can be described by the Drude model [57]

$$\varepsilon_\mathrm{E} = \varepsilon_\infty - \frac{\omega_\mathrm{P}^2}{\omega^2 + i\gamma\omega}, \tag{10}$$

where ε_∞ denotes the high-frequency relative permittivity, ω_P denotes the plasma angular frequency, and γ denotes the damping angular frequency. By fitting the experimental data, the values of the parameters can be obtained: $\varepsilon_\infty = 4$, $\hbar\omega_\mathrm{P} = 2.03$ eV, and $\hbar\gamma = 0.0827$ eV [57].

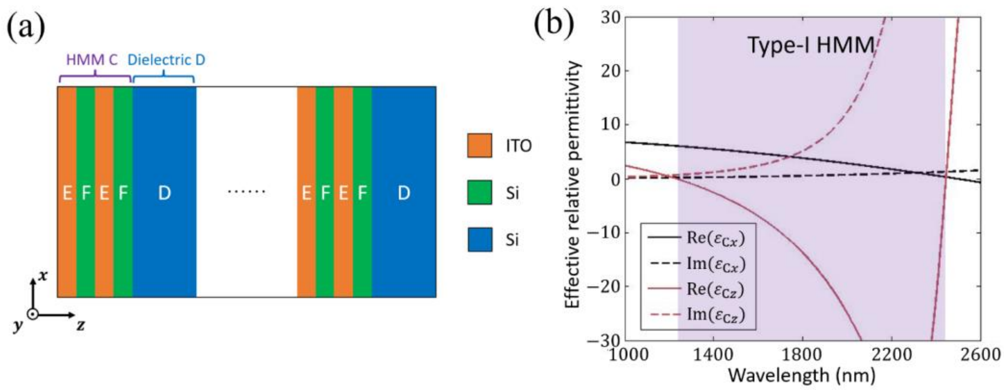

Figure 4. (**a**) Schematic of the 1-D PCCH $[(\mathrm{EF})^2\mathrm{D}]^6$, where $(\mathrm{EF})^2$ represents the HMM and D represents the dielectric. (**b**) x and z components of the effective relative permittivity tensor of the subwavelength ITO/Si multilayer $(\mathrm{EF})^2$ as a function of the wavelength. The purple shadow region represents the type-I HMM region.

According to the effective medium theory, the effective relative permittivity tensor of the subwavelength ITO/Si multilayer $(\mathrm{EF})^2$ can be expressed as [54]

$$\overset{=}{\varepsilon}_\mathrm{C} = \begin{bmatrix} \varepsilon_{\mathrm{C}x} & 0 & 0 \\ 0 & \varepsilon_{\mathrm{C}x} & 0 \\ 0 & 0 & \varepsilon_{\mathrm{C}z} \end{bmatrix}, \tag{11}$$

where

$$\varepsilon_{\mathrm{C}x} = f\varepsilon_\mathrm{E} + (1-f)\varepsilon_\mathrm{F}, \tag{12}$$

$$1/\varepsilon_{\mathrm{C}z} = f/\varepsilon_\mathrm{E} + (1-f)/\varepsilon_\mathrm{F}. \tag{13}$$

Here $f = d_\mathrm{E}/(d_\mathrm{E} + d_\mathrm{F})$ represents the filling ratio of the subwavelength ITO layer within the HMM. In the design, we select $f = 0.5$. According to Equations (12) and (13), we calculate the x and the z components of the effective relative permittivity tensor of the subwavelength ITO/Si multilayer $(\mathrm{EF})^2$ as a function of the wavelength, as shown in Figure 4b. It can be seen that the type-I HMM conditions $\mathrm{Re}(\varepsilon_{\mathrm{C}x}) > 0$ and $\mathrm{Re}(\varepsilon_{\mathrm{C}z}) < 0$ are satisfied in the wavelength range from 1229.5 to 2445.6 nm (shown by the purple shadow region in Figure 4b). Hence, the subwavelength ITO/Si multilayer $(EF)^2$ can be viewed as a type-I HMM in the wavelength range from 1229.5 to 2445.6 nm.

Now, we briefly explain why angle-insensitive PBG can be realized in such 1-D PCCH according to [46]. Substituting the relative permittivity tensor of HMM C [Equation (11)] into the Maxwell equations, we can obtain the equation of the IFC of HMM C under TM polarization [54]

$$\frac{k_x^2}{\varepsilon_{Cz}} + \frac{k_{Cz}^2}{\varepsilon_{Cx}} = k_0^2 = \left(\frac{2\pi}{\lambda}\right)^2. \tag{14}$$

Since $\mathrm{Re}(\varepsilon_{Cx}) > 0$ and $\mathrm{Re}(\varepsilon_{Cz}) < 0$, the IFC of HMM C is a hyperbola, as schematically shown by the purple solid curves in Figure 5a. As the incident angle increases, the x component of the wave vector k_x also increases, giving rise to the increase in the z component of the wave vector within HMM C k_{Cz}. Therefore, we have $\partial k_{Cz}/\partial\theta > 0$. Substituting the relative permittivity of dielectric D (ε_D) into the Maxwell equations, we can obtain the equation of the IFC of dielectric D under TM polarization [54]

$$\frac{k_x^2}{\varepsilon_D} + \frac{k_{Dz}^2}{\varepsilon_D} = k_0^2 = \left(\frac{2\pi}{\lambda}\right)^2. \tag{15}$$

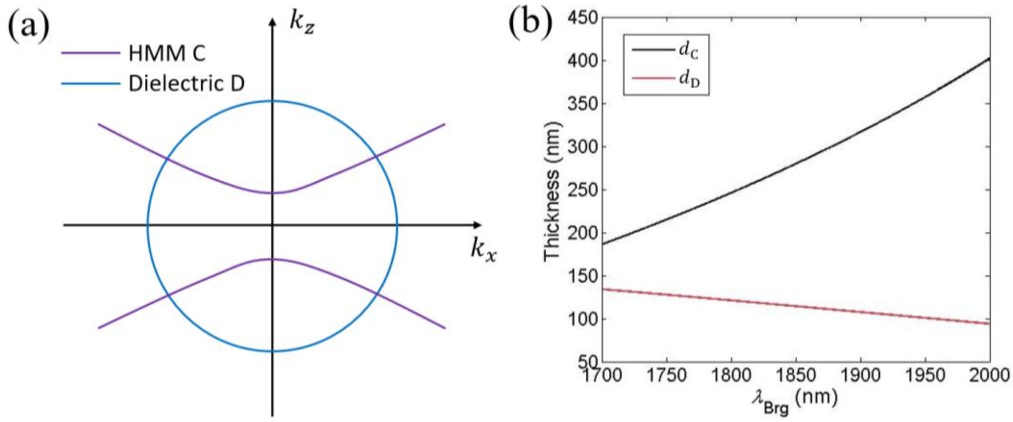

Figure 5. (**a**) IFCs of HMM C and dielectric D under TM polarization. (**b**) Thicknesses of HMM (C layer) and dielectric (D layer) as a function of the Bragg wavelength.

Clearly, the IFC of dielectric D is a circle, as schematically shown by the blue solid curve in Figure 5a. As the incident angle increases, the x component of the wave vector k_x also increases, giving rise to the decrease in the z component of the wave vector within dielectric D k_{Dz}. Therefore, we have $\partial k_{Dz}/\partial\theta < 0$. Since $\partial k_{Cz}/\partial\theta > 0$ and $\partial k_{Dz}/\partial\theta < 0$, it is possible to realize $\partial\Phi/\partial\theta = 0$ according to Equation (3) [46]. It is known that $k_z d$ represents the propagating phase within a single layer. Hence, $\partial\Phi/\partial\theta = 0$ is also called the phase-variation compensation condition [46]. When $\partial\Phi/\partial\theta = 0$, the total propagating phase within a unit cell of the 1-D PCCH is insensitive to the incident angle. As a consequence, the Bragg wavelength satisfying the Bragg condition is also angle-insensitive, giving rise to an angle-insensitive PBG. To meet the phase-variation compensation condition, the thicknesses of HMM (C layer) and dielectric (D layer) should satisfy [46]

$$d_C = \frac{\lambda_{Brg}}{2} \frac{1}{\sqrt{\varepsilon_D}\left[1 - \frac{\mathrm{Re}(\varepsilon_{Cz})}{\varepsilon_D}\right]}, \tag{16}$$

$$d_D = \frac{\lambda_{Brg}}{2} \frac{1}{\sqrt{\mathrm{Re}(\varepsilon_{Cx})}\left[1 - \frac{\varepsilon_D}{\mathrm{Re}(\varepsilon_{Cz})}\right]}. \tag{17}$$

where λ_{Brg} denotes the designed Bragg wavelength, $\mathrm{Re}(\varepsilon_{\mathrm{C}x})$ and $\mathrm{Re}(\varepsilon_{\mathrm{C}z})$ are valued at the designed Bragg wavelength. It should be noted that Equations (16) and (17) are derived under two approximate conditions $|\mathrm{Re}(\varepsilon_{\mathrm{C}z})| \gg 1$ and $\varepsilon_{\mathrm{D}} \gg 1$ [46]. Figure 5b gives the thicknesses of HMM (C layer) and dielectric (D layer) as a function of the Bragg wavelength. In the design, we select the Bragg wavelength as $\lambda_{\mathrm{Brg}} = 1844.8$ nm and obtain the thicknesses of C and D layers: $d_{\mathrm{C}} = 276.0$ nm and $d_{\mathrm{D}} = 115.0$ nm. Since $f = 0.5$, we can finally obtain the thicknesses of the subwavelength ITO and Si layers $d_{\mathrm{E}} = d_{\mathrm{F}} = 69.0$ nm.

According to the above design, we calculate the absorptance spectra of the designed 1-D PCCH $[(\mathrm{EF})^2\mathrm{D}]^6$ at different incident angles 0°, 30°, and 60° under TM polarization, as shown in Figure 6a. It should be noted that we use the realistic subwavelength multilayer structure $(\mathrm{EF})^2$ but not the homogeneous layer with the effective relative tensor in the calculation on the absorptance spectra. The incident medium is set to be air and the exit medium (substrate) is set to be BK7 glass with a refractive index $n_{\mathrm{S}} = 1.515$ [52]. One can see that a PBG emerges around the designed Bragg wavelength $\lambda_{\mathrm{Brg}} = 1844.8$ nm. Two absorptance peaks emerge at the short- and the long-wavelength band edges. Specifically, the peak values of two absorptance peaks reach 0.951 and 0.379. Interestingly, the positions of two absorptance peaks are angle-insensitive. Figure 6b also gives the group refractive index spectra of the designed 1-D PCCH $(\mathrm{AB})^{10}$ $[(\mathrm{EF})^2\mathrm{D}]^6$ at different incident angles 0°, 30°, and 60° under TM polarization. As demonstrated, at two band edges, the group refractive indices are greatly enhanced to 5.272 and 8.105, respectively. The corresponding group velocities are only 0.190c and 0.123c, respectively. Besides, two group refractive index peaks exhibit angle-insensitive property. Such angle-insensitive property of the light slowing effect gives rise to the angle-insensitive property of the absorptance peaks.

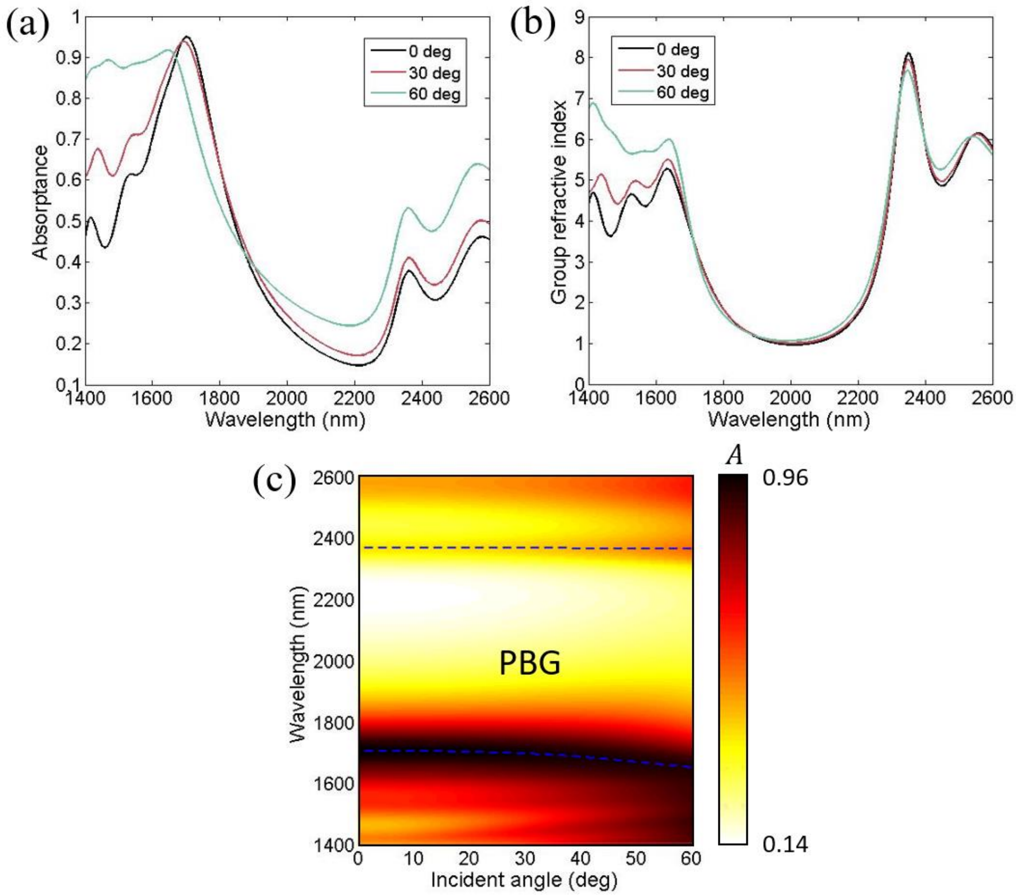

Figure 6. (**a**) Absorptance and (**b**) group refractive index spectra of the designed 1-D PCCH $[(\mathrm{EF})^2\mathrm{D}]^6$ at different incident angles 0°, 30°, and 60° under TM polarization. (**c**) Absorptance spectrum of the designed 1-D PCCH $[(\mathrm{EF})^2\mathrm{D}]^6$ as a function of the incident angle under TM polarization.

To further see the angle-dependence of two absorptance peaks, we also calculate the absorptance spectrum of the designed 1-D PCCH $[(EF)^2D]^6$ as a function of the incident angle under TM polarization, as shown in Figure 6c. The blue dashed lines represent the positions of two absorptance peaks. As the incident angle increases from 0° to 60°, the short-wavelength absorptance peak slightly shifts from 1702.0 to 1647.0 nm and the long-wavelength absorptance peak slightly shifts from 2362.3 to 2360.3 nm. The short-wavelength band edge shows a slight blueshift. The reason is that the approximate condition $|\mathrm{Re}(\varepsilon_{Cz})| \gg 1$ is not satisfied well at the short-wavelength band edge [46]. Compared with the absorptance peaks in the traditional all-dielectric 1-D PC (see Figure 2a), the absorptance peaks in the designed 1-D PCCH exhibit superior angle-insensitive property, which gives us an opportunity to achieve wide-angle absorption.

Then, we utilize the short-wavelength angle-insensitive absorptance peak to achieve wide-angle absorption. Figure 7 shows the absorptance of the designed 1-D PCCH $[(EF)^2D]^6$ as a function of the incident angle at the short-wavelength angle-insensitive band edge $\lambda = 1702.0$ nm under TM polarization. One can see that as the incident angle increases from 0° to 45°, the absorptance decreases smoothly from 0.951 to 0.902. Even at a large incident angle of 80°, the absorptance still reaches 0.444. The absorptance keeps higher than 0.9 in a wide angle range from 0° to 45.5° and keeps higher than 0.8 in a wide angle range from 0° to 61.3°. The angular average absorptance in the angle range from 0° to 90° reaches $\overline{A} = 0.788$, which is much higher than that in the traditional all-dielectric 1-D PC. Based on the angle-insensitive light slowing effect at the short-wavelength angle-insensitive band edge in the designed 1-D PCCH, we achieve wide-angle absorption at near-infrared wavelengths. It should be pointed out that the mechanism to achieve wide-angle absorption in our work is applicable in other wavelength ranges since the phase-variation compensation theory is independent to the wavelength range.

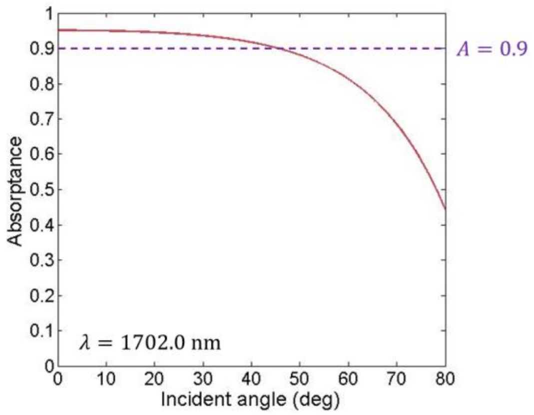

Figure 7. Absorptance of the designed 1-D PCCH $[(EF)^2D]^6$ as a function of the incident angle at the short-wavelength angle-insensitive band edge $\lambda = 1702.0$ nm under TM polarization.

Finally, we discuss whether the wide-angle absorption is robust when the phase-variation compensation condition is slightly broken. First, we reduce the thickness of C layer by 5%, i.e., $d'_C = (1 - 5\%)d_C$ while keeping the thickness of D layer unchanged, i.e., $d'_D = d_D$. Figure 8a gives the absorptance spectrum of the 1-D PCCH $[(EF)^2D]^6$ as a function of the incident angle under TM polarization. One can see that the positions of two absorptance peaks are still angle-insensitive. As the incident angle increases from 0° to 60°, the short-wavelength absorptance peak slightly shifts from 1668.9 to 1613.1 nm and the long-wavelength absorptance peak slightly shifts from 2314.0 to 2312.3 nm. Figure 8b gives the absorptance of the 1-D PCCH $[(EF)^2D]^6$ as a function of the incident angle at the short-wavelength angle-insensitive band edge $\lambda = 1668.9$ nm under TM polarization. The absorptance keeps higher than 0.9 in a wide angle range from 0° to 38.6°. The angular average absorptance in the angle range from 0° to 90° still reaches $\overline{A} = 0.769$. Similarly, we keep the thickness of C layer unchanged, i.e., $d''_C = d_C$ while reduce the thickness of

D layer by 5%, i.e., $d''_{\mathrm{D}} = (1-5\%)d_{\mathrm{D}}$. Figure 8c gives the absorptance spectrum of the 1-D PCCH $[(\mathrm{EF})^2\mathrm{D}]^6$ as a function of the incident angle under TM polarization. One can see that the positions of two absorptance peaks are still angle-insensitive. As the incident angle increases from 0° to 60°, the short-wavelength absorptance peak slightly shifts from 1668.0 to 1634.0 nm and the long-wavelength absorptance peak slightly shifts from 2319.7 to 2319.4 nm. Figure 8d gives the absorptance of the 1-D PCCH $[(\mathrm{EF})^2\mathrm{D}]^6$ as a function of the incident angle at the short-wavelength angle-insensitive band edge $\lambda = 1668.0$ nm under TM polarization. The absorptance keeps higher than 0.9 in a wide angle range from 0° to 44.3°. The angular average absorptance in the angle range from 0° to 90° still reaches $\overline{A} = 0.786$. To sum up, the wide-angle absorption is robust when the phase-variation compensation condition is slightly broken.

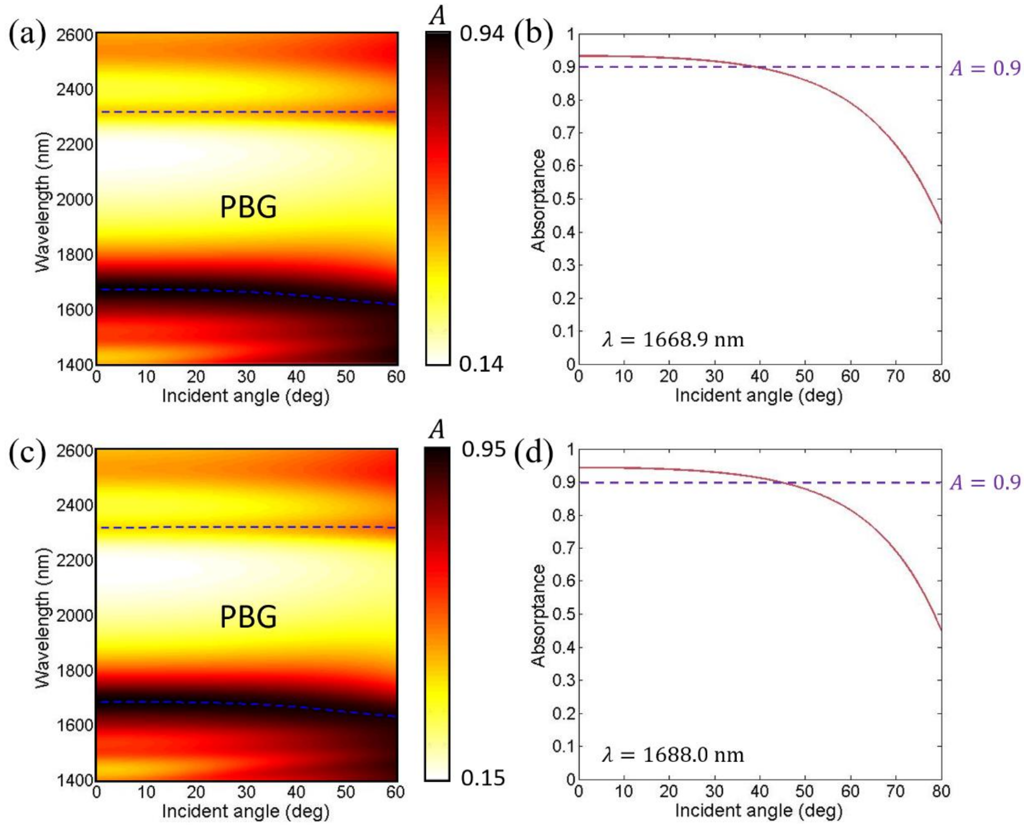

Figure 8. (**a**) Absorptance spectrum of the 1-D PCCH $[(\mathrm{EF})^2\mathrm{D}]^6$ as a function of the incident angle under TM polarization when $d'_{\mathrm{C}} = (1-5\%)d_{\mathrm{C}}$ and $d'_{\mathrm{D}} = d_{\mathrm{D}}$. (**b**) Absorptance of the 1-D PCCH $[(\mathrm{EF})^2\mathrm{D}]^6$ as a function of the incident angle at the short-wavelength angle-insensitive band edge $\lambda = 1668.9$ nm under TM polarization when $d'_{\mathrm{C}} = (1-5\%)d_{\mathrm{C}}$ and $d'_{\mathrm{D}} = d_{\mathrm{D}}$. (**c**) Absorptance spectrum of the 1-D PCCH $[(\mathrm{EF})^2\mathrm{D}]^6$ as a function of the incident angle under TM polarization when $d''_{\mathrm{C}} = d_{\mathrm{C}}$ and $d''_{\mathrm{D}} = (1-5\%)d_{\mathrm{D}}$. (**d**) Absorptance of the 1-D PCCH $[(\mathrm{EF})^2\mathrm{D}]^6$ as a function of the incident angle at the short-wavelength angle-insensitive band edge $\lambda = 1668.0$ nm under TM polarization when $d''_{\mathrm{C}} = d_{\mathrm{C}}$ and $d''_{\mathrm{D}} = (1-5\%)d_{\mathrm{D}}$.

4. Conclusions

In summary, we design an angle-insensitive PBG in a 1-D PCCH based on the phase-variation compensation theory. Assisted by the angle-insensitive light slowing effect at the angle-insensitive band edge, we realize wide-angle absorption at near-infrared wavelengths. At the short-wavelength angle-insensitive band edge ($\lambda = 1702.0$ nm), the absorptance keeps higher than 0.9 in a wide angle range from 0° to 45.5°. The angular average absorptance in the angle range from 0° to 90° reaches $\overline{A} = 0.788$, which is much higher than that in the traditional all-dielectric 1-D PC. Besides, the wide-angle absorption is robust when the phase-variation compensation condition is slightly broken. These results not only provide a viable route to realize angle-insensitive light slowing and wide-angle light absorption, but also promote the development of light-slowing- and absorption-based optical/optoelectronic devices.

Author Contributions: Conceptualization, F.W.; methodology, F.W.; software, F.W., X.L., X.F. and L.L.; validation, F.W.; formal analysis, F.W., X.L., X.F. and L.L.; investigation, F.W.; resources, F.W.; data curation, F.W. and X.L.; writing—original draft preparation, F.W.; writing—review and editing, F.W., S.A.T. and A.P.; visualization, F.W.; supervision, F.W.; project administration, F.W.; funding acquisition, F.W. All authors have read and agreed to the published version of the manuscript.

Funding: This research was funded by National Natural Science Foundation of China (12104105) and Start-up Funding of Guangdong Polytechnic Normal University (2021SDKYA033).

Institutional Review Board Statement: Not applicable.

Informed Consent Statement: Not applicable.

Data Availability Statement: Not applicable.

Conflicts of Interest: The authors declare no conflict of interest.

References

1. Tomić, S.; Jones, T.S.; Harrison, N.M. Absorption characteristics of a quantum dot array induced intermediate band: Implications for solar cell design. *Appl. Phys. Lett.* **2008**, *93*, 263105. [CrossRef]
2. Li, Q.; Lu, J.; Gupta, P.; Qiu, M. Engineering optical absorption in graphene and other 2D materials: Advances and applications. *Adv. Opt. Mater.* **2019**, *7*, 1900595. [CrossRef]
3. Li, Y.; Poon, A.W. Active resonance wavelength stabilization for silicon microring resonators with an in-resonator defect-state-absorption-based photodetector. *Opt. Express* **2015**, *23*, 360–372. [CrossRef] [PubMed]
4. Du, W.; Yu, P.; Zhu, J.; Li, C.; Xu, H.; Zou, J.; Wu, C.; Wen, Q.; Ji, H.; Liu, T.; et al. An ultrathin $MoSe_2$ photodetector with near-perfect absorption. *Nanotechnology* **2020**, *31*, 225201. [CrossRef]
5. Xu, K.; Li, H.; Liu, Y.; Wang, Y.; Tian, J.; Wang, L.; Du, J.; He, Z.; Song, Q. Optical fiber humidity sensor based on water absorption peak near 2-μm waveband. *IEEE Photonics J.* **2019**, *11*, 7101308. [CrossRef]
6. Chen, Y.; Fan, Y.; Zhang, Z.; Zhu, Z.; Liu, K.; Zhang, J.; Xu, W.; Yuan, X.; Guo, C. High-resolution graphene angle sensor based on ultra-narrowband optical perfect absorption. *Opt. Express* **2021**, *29*, 41206–41212. [CrossRef]
7. Ito, K.; Saheki, T.; Murakami, Y.; Taniguchi, I.; Kikuchi, M.; Unosawa, Y. A novel gas analyzer for SO_2, NO and NO_2 in the stack effluent. *Jpn. J. Appl. Phys.* **1975**, *14*, 131. [CrossRef]
8. Konopelko, L.A.; Tyurikova, E.P.; Snytko, Y.N. Investigation of spectral characteristics of an optical-absorption gas analyzer for monitoring freons in the air. *Opt. Spectrosc.* **2020**, *128*, 678–685. [CrossRef]
9. Schurig, D.; Mock, J.J.; Justice, B.J.; Cummer, S.A.; Pendry, J.B.; Starr, A.F.; Smith, D.R. Metamaterial electromagnetic clock at microwave frequencies. *Science* **2006**, *314*, 977–980. [CrossRef]
10. Cui, Y.; Fung, K.H.; Xu, J.; Ma, H.; Jin, Y.; He, S.; Fang, N.X. Ultrabroadband light absorption by a sawtooth anisotropic metamaterial slab. *Nano. Lett.* **2012**, *12*, 1443–1447. [CrossRef]
11. Landy, N.I.; Sajuyigbe, S.; Mock, J.J.; Smith, D.R.; Padilla, W.J. Perfect metamaterial absorber. *Phys. Rev. Lett.* **2008**, *100*, 207402. [CrossRef] [PubMed]
12. Xia, S.; Zhai, X.; Huang, Y.; Liu, J.; Wang, L.; Wen, S. Multi-band perfect plasmonic absorptions using rectangular graphene gratings. *Opt. Lett.* **2017**, *42*, 3052–3055. [CrossRef] [PubMed]
13. Tian, J.; Luo, H.; Li, Q.; Pei, X.; Du, K.; Qiu, M. Near-infrared super-absorbing all-dielectric metasurface based on single-layer germanium nanostructures. *Laser Photonics Rev.* **2018**, *12*, 1800076. [CrossRef]
14. Vyunishev, A.M.; Bikbaev, R.G.; Svyakhovskiy, S.E.; Timofeev, I.V.; Pankin, P.S.; Evlashin, S.A.; Vetrov, S.Y.; Myslivets, S.A.; Arkhipkin, V.G. Broadband Tamm plasmon polariton. *J. Opt. Soc. Am. B* **2019**, *36*, 2299–2305. [CrossRef]
15. Cai, Y.; Guo, Y.; Zhou, Y.; Huang, X.; Yang, G.; Zhu, J. Tunable dual-band terahertz absorber with all-dielectric configuration based on graphene. *Opt. Express* **2020**, *28*, 31524–31534. [CrossRef] [PubMed]
16. Baqir, M.A. Conductive metal-oxide-based tunable, wideband, and wide-angle metamaterial absorbers operating in the near-infrared and short-wavelength infrared regions. *Appl. Opt.* **2020**, *59*, 10912–10919. [CrossRef] [PubMed]
17. Tian, J.; Li, Q.; Belov, P.A.; Sinha, R.K.; Qian, W.; Qiu, M. High-*Q* all-dielectric metasurface: Super and suppressed optical absorption. *ACS Photonics* **2020**, *7*, 1436–1443. [CrossRef]
18. Guan, J.; Xia, S.; Zhang, Z.; Wu, J.; Meng, H.; Yue, J.; Zhai, X.; Wang, L.; Wen, S. Two switchable plasmonically induced transparency effects in a system with distinct graphene resonators. *Nanoscale Res. Lett.* **2020**, *15*, 142. [CrossRef] [PubMed]
19. Zhang, Y.; Wu, Z.; Cao, Y.; Zhang, H. Optical properties of one-dimensional Fibonacci quasi-periodic graphene photonic crystal. *Opt. Commun.* **2015**, *338*, 168–173. [CrossRef]

20. Lee, J.; Min, K.; Park, Y.; Cho, K.; Jeon, H. Photonic crystal phosphors integrated on a blue LED chip for efficient white light generation. *Adv. Mater.* **2018**, *30*, 1703506. [CrossRef] [PubMed]
21. Huang, S.; Kato, M.; Kuramochi, E.; Lee, C.; Notomi, M. Time-domain and spectral-domain investigation of inflection-point slow-light modes in photonic crystal coupled waveguides. *Opt. Express* **2007**, *15*, 3543–3549. [CrossRef] [PubMed]
22. Goldring, D.; Levy, U.; Dotan, I.E.; Tsukernik, A.; Oksman, M.; Rubin, I.; David, Y.; Mendlovic, D. Experimental measurement of quality factor enhancement using slow light modes in one dimensional photonic crystal. *Opt. Express* **2008**, *16*, 5585–5595. [CrossRef] [PubMed]
23. Torrijos-Morán, L.; Griol, A.; García-Rupérez, J. Slow light bimodal interferometry in one-dimensional photonic crystal waveguides. *Light Sci. Appl.* **2021**, *10*, 16. [CrossRef] [PubMed]
24. Wu, F.; Wu, X.; Xiao, S.; Liu, G.; Li, H. Broadband wide-angle multilayer absorber based on a broadband omnidirectional optical Tamm state. *Opt. Express* **2021**, *29*, 23976–23987. [CrossRef]
25. Wang, Z.; Ou, Y.; Wang, S.; Meng, Y.; Wang, Z.; Zhai, X.; Wang, L.; Xia, S. Ultrahigh-Q tunable terahertz absorber based on bulk Dirac semimetal with surface lattice resonance. *Photonics* **2022**, *9*, 22. [CrossRef]
26. Lin, S.; Fleming, J.G.; El-Kady, I. Experimental observation of photonic-crystal emission near a photonic band edge. *Appl. Phys. Lett.* **2003**, *83*, 593–595. [CrossRef]
27. Lin, S.Y.; Fleming, J.G.; Li, Z.Y.; El-Kady, I.; Biswas, R.; Ho, K.M. Origin of absorption enhancement in a tungsten, three-dimensional photonic crystal. *J. Opt. Soc. Am. B* **2003**, *20*, 1538–1541. [CrossRef]
28. Fink, Y.; Winn, J.N.; Fan, S.; Chen, C.; Michel, J.; Joannopoulos, J.D.; Thomas, E.L. A dielectric omnidirectional reflector. *Science* **1998**, *282*, 1679–1682. [CrossRef]
29. Kaliteevski, M.; Iorsh, I.; Brand, S.; Abram, R.A.; Chamberlain, J.M.; Kavokin, A.V.; Shelykh, I.A. Tamm plasmon-polaritons: Possible electromagnetic states at the interface of a metal and a dielectric Bragg mirror. *Phys. Rev. B* **2007**, *76*, 165415. [CrossRef]
30. Wan, B.; Xu, Y.; Zhou, Z.; Zhang, D.; Zhang, H. Theoretical investigation of a sensor based on one-dimensional photonic crystals to measure four physical quantities. *IEEE Sens. J.* **2020**, *21*, 2846–2853. [CrossRef]
31. Panda, A.; Pukhrambam, P.D. Investigation of defect based 1D photonic crystal structure for real-time detection of waterborne bacteria. *Phys. B* **2021**, *607*, 412854. [CrossRef]
32. Kaňok, R.; Hlubina, P.; Gembalová, L.; Ciprian, D. Efficient optical sensing based on phase shift of waves supported by a one-dimensional photonic crystal. *Sensors* **2021**, *21*, 6535. [CrossRef]
33. Wang, F.; Cheng, Y.Z.; Wang, X.; Qi, D.; Luo, X.; Gong, R.Z. Effective modulation of the photonic band gap based on Ge/ZnS one-dimensional photonic crystal at the infrared band. *Opt. Mater.* **2018**, *75*, 373–378. [CrossRef]
34. Jena, S.; Tokas, R.B.; Sarkar, P.; Misal, J.S.; Haque, S.M.; Rao, K.D.; Thakur, S.; Sahoo, N.K. Omnidirectional photonic band gap in magnetron sputtered TiO_2/SiO_2 one-dimensional photonic crystal. *Thin Solid Film.* **2016**, *599*, 138–144. [CrossRef]
35. Kong, X.; Liu, S.; Zhang, H.; Li, C.; Bian, B. Omnidirectional photonic band gap of one-dimensional ternary plasma photonic crystals. *J. Opt.* **2011**, *13*, 035101. [CrossRef]
36. Trabelsi, Y.; Belhadj, W.; Ali, N.B.; Aly, A.H. Theoretical study of tunable optical resonators in periodic and quasiperiodic one-dimensional photonic structures incorporating a nematic liquid crystal. *Photonics* **2021**, *8*, 150. [CrossRef]
37. Panda, A.; Pukhrambam, P.D.; Wu, F.; Belhadj, W. Graphene-based 1D defective photonic crystal biosensor for real-time detection of cancer cells. *Eur. Phys. J. Plus* **2021**, *136*, 809. [CrossRef]
38. Zhukovsky, S.V.; Orlov, A.A.; Babicheva, V.E.; Lavrinenko, A.V.; Sipe, J.E. Photonic-band-gap engineering for volume plasmon polaritons in multiscale multilayer hyperbolic metamaterials. *Phys. Rev. A* **2014**, *90*, 013801. [CrossRef]
39. Wu, F.; Lu, G.; Guo, Z.; Jiang, H.; Xue, C.; Zheng, M.; Chen, C.; Du, G.; Chen, H. Redshift gaps in one-dimensional photonic crystals containing hyperbolic metamaterials. *Phys. Rev. Appl.* **2018**, *10*, 064022. [CrossRef]
40. Wu, F.; Lyu, K.; Hu, S.; Yao, M.; Xiao, S. Ultra-large omnidirectional photonic band gaps in one-dimensional ternary photonic crystals composed of plasma, dielectric and hyperbolic metamaterial. *Opt. Mater.* **2021**, *111*, 110680. [CrossRef]
41. Xia, J.; Chen, Y.; Xiang, Y. Enhanced spin Hall effect due to the redshift gaps of photonic hypercrystals. *Opt. Express* **2021**, *29*, 12160–12168. [CrossRef]
42. Tumkus, T.; Zhu, G.; Black, P.; Barnakov, Y.A.; Bonner, C.E.; Noginov, M.A. Control of spontaneous emission in a volume of functionalized hyperbolic metamaterial. *Appl. Phys. Lett.* **2011**, *99*, 151115. [CrossRef]
43. Wang, Z.; Zhang, Z.M.; Quan, X.; Cheng, P. A perfect absorber design using a natural hyperbolic material for harvesting solar energy. *Sol. Energy* **2018**, *159*, 329–336. [CrossRef]
44. Qi, H.; Sang, T.; Wang, L.; Yin, X.; Wang, J.; Wang, Y. Dual-band light absorption enhancement in hyperbolic rectangular array. *Appl. Sci.* **2019**, *9*, 2011. [CrossRef]
45. Janaszek, B.; Szczepański, P. Distributed feedback laser based on tunable photonic hypercrystal. *Materials* **2021**, *14*, 4065. [CrossRef]
46. Xue, C.; Ding, Y.; Jiang, H.; Li, Y.; Wang, Z.; Zhang, Y.; Chen, H. Dispersionless gaps and cavity modes in photonic crystals containing hyperbolic metamaterials. *Phys. Rev. B* **2016**, *93*, 125310. [CrossRef]
47. Wu, F.; Lu, G.; Xue, C.; Jiang, H.; Guo, Z.; Zheng, M.; Chen, C.; Du, G.; Chen, H. Experimental demonstration of angle-independent gaps in one-dimensional photonic crystals containing layered hyperbolic metamaterials and dielectrics at visible wavelengths. *Appl. Phys. Lett.* **2018**, *112*, 041902. [CrossRef]

48. Shen, K.; Li, X.; Zheng, Y.; Liu, H.; Dong, S.; Zhang, J.; Xia, S.; Dong, C.; Sun, X.; Zhang, X.; et al. Near-infrared ITO-based photonic hypercrystals with large angle-insensitive bandgaps. *Opt. Lett.* **2022**, *47*, 917–920. [CrossRef]
49. Zhang, B.; Zhao, Y.; Hao, Q.; Kiraly, B.; Khoo, I.C.; Chen, S.; Huang, T.J. Polarization-independent dual-band infrared perfect absorber based on a metal-dielectric-metal elliptical nanodisk array. *Opt. Express* **2011**, *19*, 15221–15228. [CrossRef] [PubMed]
50. He, Z.; Wu, L.; Liu, Y.; Lu, Y.; Wang, F.; Shao, W.; Fu, S.; Tong, G. Ultrawide bandwidth and large-angle electromagnetic wave absorption based on triple-nested helix metamaterial absorbers. *J. Appl. Phys.* **2020**, *127*, 174901. [CrossRef]
51. Yeh, P. *Optical Waves in Layered Media*; Wiley: Hoboken, NJ, USA, 1988.
52. Dominici, L.; Michelotti, F.; Brown, T.M.; Reale, A.; Carlo, A.D. Plasmon polaritons in the near infrared on fluorine doped tin oxide films. *Opt. Express* **2009**, *17*, 10155–10167. [CrossRef]
53. Xu, P.; Tian, H.P.; Ji, Y.F. One-dimensional fractal photonic crystal and its characteristics. *J. Opt. Soc. Am. B* **2010**, *27*, 640–647. [CrossRef]
54. Ferrari, L.; Wu, C.; Lepage, D.; Zhang, X.; Liu, Z. Hyperbolic metamaterials and their applications. *Prog. Quantum Electron.* **2015**, *40*, 1–40. [CrossRef]
55. Li, J.; Zhou, L.; Chan, C.T.; Sheng, P. Photonic band gap from a stack of positive and negative index materials. *Phys. Rev. Lett.* **2003**, *90*, 083901. [CrossRef]
56. Palik, E. *Handbook of Optical Constants of Solids*; Academic: New York, NY, USA, 1998.
57. Losego, M.D.; Efremenko, A.Y.; Rhodes, C.L.; Cerruti, M.G.; Franzen, S.; Maria, J. Conductive oxide thin films: Model systems for understanding better plasmonic materials. *J. Appl. Phys.* **2009**, *106*, 024903. [CrossRef]